

# Tunable magnetocaloric effect and enhanced refrigerant capacity in composite-like oxide heterostructures

M. Abbasi Eskandari,<sup>1</sup> S.S. Ghotb,<sup>1</sup> M. Balli,<sup>2</sup> and P. Fournier<sup>1</sup>

<sup>1</sup>*Institut quantique, Regroupement québécois sur les matériaux de pointe et Département de physique, Université de Sherbrooke, Sherbrooke, J1K 2R1, Québec, Canada*

<sup>2</sup>*LERMA, ECINE, International University of Rabat, Parc Technopolis, Rocade de Rabat-Salé, 11100, Morocco*

We report a detailed study of the magnetocaloric effect in heterostructures of  $\text{La}_2\text{NiMnO}_6$  and  $\text{La}_{2/3}\text{Sr}_{1/3}\text{MnO}_3$ . The shape, width and magnitude of the temperature dependence of the magnetic entropy change ( $\Delta S_m$ ) for these multilayer samples can be tuned and controlled by changing their layout. A large  $\Delta S_m$  over a wide temperature range which goes beyond room temperature is observed in all samples. We observe a temperature-independent table-top-like  $\Delta S_m$  over a temperature range as large as 100 K in the trilayer samples.  $\text{La}_2\text{NiMnO}_6$  double perovskite with multiple magnetic phase transitions is the key to tuning and shaping the temperature dependence of the magnetic entropy changes to suit the requirements of several cooling cycles.

## I. INTRODUCTION

Magnetic refrigeration technology based on the magnetocaloric effect (MCE) has been under the spotlight due to its advantages over the conventional gas compression technology, such as higher energy efficiency and being eco-friendly [1, 2]. The MCE is an intrinsic property of magnetic materials and it is defined as the heating or cooling of a magnetic substance as it is magnetized or demagnetized, respectively. The MCE was first reported in 1917 by P. Weiss and A. Piccard in nickel close to its paramagnetic to ferromagnetic transition temperature. They noted that Ni would warm up or cool down when magnetized or demagnetized [3]. Isothermal magnetic entropy change ( $\Delta S_m$ ) and adiabatic temperature change ( $\Delta T_{ad}$ ) are two parameters that are mostly used in order to characterize the potential of a magnetocaloric material.  $\Delta S_m$  and  $\Delta T_{ad}$  indicate the amount of heat that can be moved during the refrigeration process and the temperature change that can be achieved, respectively. They can be measured using specific heat or magnetization. In the late 1970s, gadolinium was introduced as the first working material for magnetic refrigeration taking advantage of its large MCE near its magnetic transition close to room temperature [4]. Gd shows a large isothermal entropy change of  $-\Delta S_m = 5.5 \text{ J kg}^{-1} \text{ K}^{-1}$  and an adiabatic temperature change of  $\Delta T_{ad} = 6 \text{ K}$  near its transition temperature at 294 K under a magnetic field of 2 T, numbers still used for comparison with novel materials. However, for an implementation in domestic cooling devices, one needs to find materials with a magnetic transition leading to a significant magnetic entropy change over a wide temperature range covering roughly from 20 °C to -20 °C. For some magnetic refrigeration cycles such as active magnetic regenerative (AMR) refrigeration, a so-called *table-top* temperature independence of the magnetic entropy change would be also a great asset [2].

A narrow working temperature range, the metallic behavior and the high cost of Gd restrict its utiliza-

tion for domestic and large scale applications. Looking for alternative solutions, many families with significant magnetocaloric effect close to room temperature such as Gd-based alloys [5, 6],  $\text{LaFe}_{13-x}\text{Si}_x$  intermetallic compounds [7–9] and manganites of general formula  $\text{R}_{1-x}\text{A}_x\text{MnO}_3$  (where R = Lanthanide and A = divalent alkaline earth) have received enormous attention due to their advantages such as tunable transition temperature using chemical manipulations and large MCE [10, 11]. For instance, magnetic and magnetocaloric properties of  $\text{La}_{1-x}\text{Sr}_x\text{MnO}_3$  (LSMO) manganites have been widely explored. It shows a high transition temperature ( $T_c$ ), as high as 370 K, with a maximum magnetic entropy change of  $1.5 \text{ J kg}^{-1} \text{ K}^{-1}$  at 1 T [12]. Despite the narrow operating temperature range ( $\Delta T_{ad}$ ) and its metallic nature driven by double exchange, a large  $\Delta S_m$  makes  $\text{La}_{1-x}\text{Sr}_x\text{MnO}_3$  a promising candidate for magnetic cooling systems at room temperature. Similarly, double perovskites with general formula  $\text{A}_2\text{BB}'\text{O}_6$  (where A is a trivalent rare earth or divalent alkaline and B and B' are transition metals) have also attracted interest [13–15]. The main advantage of double perovskites over manganites is their higher electrical resistivity [16, 17].  $\text{La}_2\text{NiMnO}_6$  (LNMO) as a near room-temperature ferromagnetic semiconductor is attracting because of its unique properties such as the existence of two magnetic phases with different transition temperatures controlled by the level of B/B' site cationic ordering [18–20]. Cation-ordered LNMO exhibits a maximum magnetic phase transition at 285 K. In this ordered phase, only ferromagnetic  $\text{Ni}^{2+}-\text{O}-\text{Mn}^{4+}$  bonds driven by superexchange exist. On the other hand, non-optimal growth conditions can lead to a mixture of ferromagnetic ( $\text{Ni}^{2+}-\text{O}-\text{Mn}^{4+}$ ) and antiferromagnetic ( $\text{Ni}^{2+}-\text{O}-\text{Ni}^{2+}$  and  $\text{Mn}^{4+}-\text{O}-\text{Mn}^{4+}$ ) bonds in a so-called cation-disordered phase. The fully disordered LNMO shows a magnetic transition at  $T_c \sim 150 \text{ K}$  [18]. This transition temperature gradually increases with the level of cationic ordering as samples oftentimes show two magnetic transitions. This unique feature allows one to

control and tune the magnetic and magnetocaloric properties in LNMO by changing the ratio of ordering in the system through variation of the growth conditions in hope of tailoring a proper MCE. For instance, Matte *et al.*, [21] investigated the effect of thin film growth conditions on the level of ordering in LNMO and consequently on magnetocaloric properties. The authors were able to control and adjust the shape and width of  $\Delta S_m$  and get a temperature-independent magnetic entropy change over a wide temperature range, as large as 100 K, by changing the ratio of ordering in LNMO, taking advantage of the two magnetic transitions in the same sample and reproducing in a sense what is expected from a composite.

As other compounds, magnetic and magnetocaloric properties of manganites and double perovskites can be tuned in the hope of achieving a large and temperature independent magnetic entropy change. In order to attain a desirable magnetic entropy change close to room temperature several routes have been widely explored such as doping with different elements and changing the growth conditions [14, 21, 22]. Another approach to control and tune the magnetocaloric properties of materials is to combine different materials in a composite structure [23–25]. In this case, materials with different transition temperatures are used to obtain a large magnetic entropy change over a wide temperature range [23, 24]. In this paper, we choose heterostructures mimicking composites to achieve a suitable magnetocaloric material at room temperature. For this purpose, we take advantage of the potential presence of tunable multiple magnetic transitions in LNMO while combining it to LSMO showing a transition above room temperature. We grow and study the properties of bilayers and trilayers with the intention of tailoring the magnetic entropy change over a wide temperature range, while taking advantage of strain effects provoked by the lattice mismatches between the substrates and the films.

## II. EXPERIMENTS AND METHODS

In this paper, two series of bilayers and trilayers of  $\text{La}_2\text{NiMnO}_6$  (LNMO) and  $\text{La}_{2/3}\text{Sr}_{1/3}\text{MnO}_3$  (LSMO) with different configurations are made on (001)-oriented LSAT substrates (Figure 1). The epitaxial bilayers and trilayers samples are grown by pulsed laser deposition (PLD) using a KrF excimer laser. The films are deposited at 800 °C, under an oxygen pressure of 200 mTorr. After the deposition, the PLD chamber is filled with oxygen up to 200 Torr, and then the films are cooled down to room temperature with a cooling rate of 10 °C/min. In the first type of bilayer samples (Fig. 1 (a)), a layer of LSMO is placed initially on the substrate and then a layer of LNMO is deposited on top: it is named B–SN. The other bilayer layout is simply the reverse (Fig. 1 (b)), with a first layer of LNMO on the substrate followed by a layer of LSMO on top (B–NS). These bilayers allow us to sort out the impact of strain on the magnetic properties caused by the lattice mismatch between the substrate

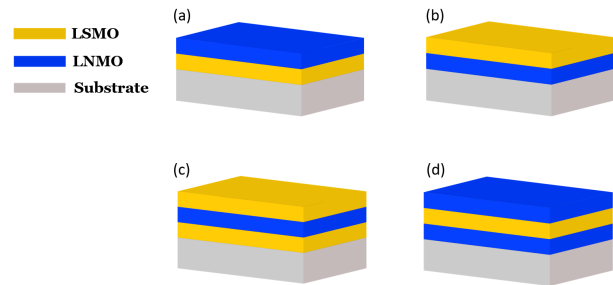


**FIG. 1:** Schematic illustration of all grown samples. (a) bilayer of LSMO-LNMO (B–SN), (b) bilayer of LNMO-LSMO (B–NS), (c) trilayer of LSMO-LNMO-LSMO (T–SNS) and (d) trilayer of LNMO-LSMO-LNMO (T–NSN).

and the films. Two different types of trilayer samples were also made. In the first trilayer samples shown in Fig. 1 (c), a layer of LNMO is sandwiched between two LSMO layers (T–SNS). Fig. 1 (d) shows the second type of trilayer samples with two LNMO layers and a middle LSMO layer (T–NSN). Each single layer of LSMO and LNMO has a thickness of 50 nm, implying that the bilayer and trilayer samples have a total thickness of 100 and 150 nm, respectively. 100 nm thick monolayers were also grown for comparison.

Room temperature x-ray diffraction (XRD) was performed using a high-resolution Bruker AXS D8-diffractometer with  $\text{CuK}_{\alpha 1}$  radiation in the  $2\theta/\omega$  configuration. The measurement of the magnetic properties are carried out using a Magnetic Property Measurement System (MPMS) from Quantum Design. In order to detect the small magnetic signals from thin films, magnetization measurements were performed using the reciprocating sample option (RSO) with an external magnetic field applied parallel to the surface of the samples. In this work, in order to determine the Arrott plots and the isothermal magnetic entropy changes ( $\Delta S_m$ ), the isothermal magnetization curves as a function of the applied field up to 7 T in the temperature range of 50 to 370 K with a temperature interval of 10 K are measured for all the samples. Figure 2 shows an example of isothermal magnetization measurements for a B–NS sample. As one may notice, all the magnetization curves show a negative slope at large field (Fig. 2 (a)) which originates from the diamagnetism of the substrate and the sample holder. As shown in Fig. 2 (b), the magnetization of layers which saturate very rapidly at low field can be clearly seen by removing this negative background. It should also be mentioned that the mass of the multilayers were estimated using the theoretical density of LSMO and LNMO, as well as the volume of the layers.

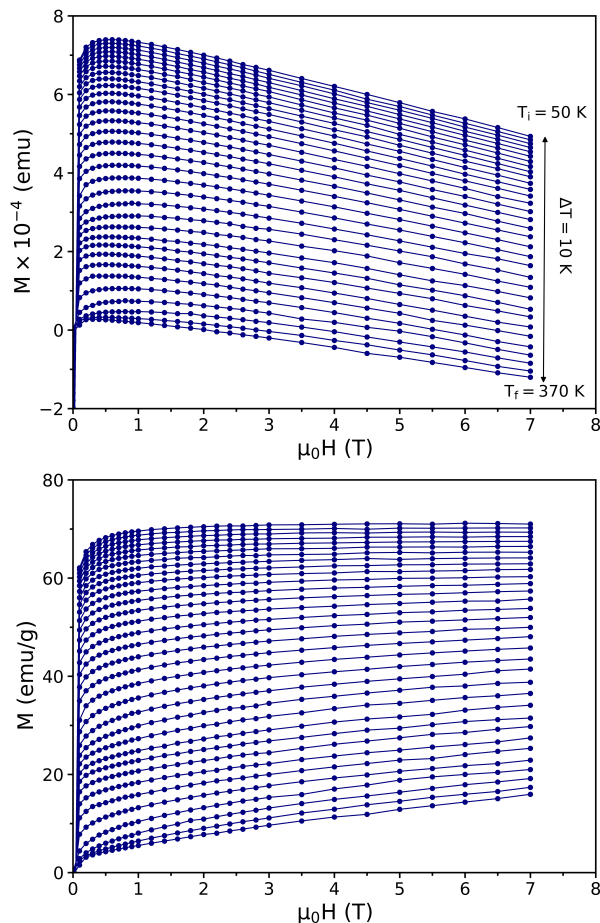


**FIG. 2:** Isothermal magnetization curves as a function of magnetic field in the temperature range from 50 to 370 K with the temperature interval of 10 K for B-NS sample; (a) Including the diamagnetic signal from the substrate and the sample holder (b) After removing the negative background.

### III. RESULTS AND DISCUSSION

Figure 3 shows the XRD patterns of all samples from  $45^\circ$  to  $48^\circ$  close to the substrate's (002) Bragg peak. The XRD patterns of 100 nm thick monolayers of LSMO and LNMO at the bottom of the figure show the proximity of their (004) diffraction peaks. In these individual spectra, the single layers of LSMO and LNMO exhibit a central peak at  $46.73^\circ$  and  $46.62^\circ$ , respectively. In both cases, their position is in part defined by the impact of strain due to their lattice mismatch with the substrate shifting their angular position with respect to the bulk [26, 27]. We are expecting strain to play also a role for thinner layers inserted in multilayers with additional shifts. Nevertheless, the growth conditions used for this work produce extremely smooth LSMO as revealed by the numerous Laue oscillations.

For the multilayers, all observed peaks can be assigned to the (00 $l$ ) crystallographic planes. It is confirming

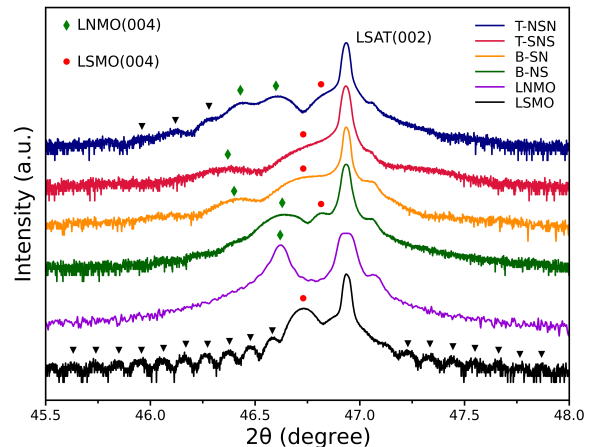


**FIG. 3:** X-ray diffraction patterns. From bottom to top: of the monolayers of LSMO and LNMO, two bilayers of B-SN and B-NS, as well as two trilayers of T-SNS and T-NSN. Laue oscillations are specified with ( $\blacktriangledown$ ). The spectra have been moved vertically for clarity.

their out-of-plane orientation and a smooth cube-on-cube growth. For bilayers, the LNMO diffraction peak for B-SN sits at a lower value of  $2\theta$  than in B-NS as its top LNMO layer is affected by the compressive strain from the bottom LSMO layer. In the supplemental material, we show the spectra close to the substrate's (001) Bragg peak. In this case, we observe Laue oscillations coming from LSMO and/or LNMO layers. The presence of these oscillations confirms the good crystalline quality of our samples with a well-defined interfaces. The top two spectra in Fig. 3 present the data for T-NSN and T-SNS trilayers. We notice the presence of three distinct peaks in the spectrum for T-NSN, where the peaks for the top and the bottom layers of LNMO coexist in the sample: their separation is the result of different strain experienced by both layers. In this particular case, we conclude in fact that the top LNMO layer is affected by a stronger compressive strain than the bottom one. Finally, the XRD spectrum for T-SNS shows only two diffraction peaks, one is associated to the middle LNMO layer, and two LSMO layers show a broad peak close to the substrate's peak.

Atomic force microscopy (AFM) data (see supplemental material) show that the surface roughness on top of the monolayers, bilayers and trilayers is on the order of 1–2 nm, 3–7 nm and 7–14 nm, respectively. In fact, variations of about 1–2 nm over lateral distances of the order of  $1\ \mu\text{m}$  for the monolayers indicate that the second and/or the third layers grow on top of a fairly smooth surface, resulting in well-defined interfaces between the layers.

In the next section the magnetic and magnetocaloric properties of bilayer and trilayer samples will be investigated in detail.

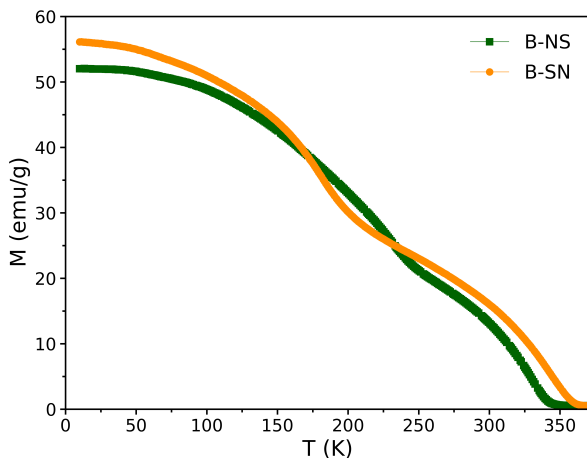


**FIG. 4:** Temperature dependence of the FC magnetization of the bilayer samples at a fixed magnetic field of 200 Oe in the temperature range between 10 to 370 K.

### A. Bilayers

Figure 4 shows field-cooled (FC) magnetization measurements as a function of temperature at a fixed magnetic field of 200 Oe for bilayer samples. Both samples undergo two magnetic phase transitions from the ferromagnetic to the paramagnetic state. In the case of the B-NS sample, a first transition at roughly 230 K comes from the LNMO layer while the other at 330 K is related to the LSMO layer. The magnetic transition of LNMO at temperatures above 200 K confirms a high but incomplete level of cation ordering at the B/B' sites in the LNMO layer sitting directly on the substrate. For B-SN layout, the magnetic transition of the LSMO layer shifts at 345 K, while the transition temperature of LNMO sitting on top of LSMO shifts down to 180 K. The lower transition temperature of the LNMO layer in this configuration indicates a lower level of cation ordering than in the previous bilayer [18]. This difference in cation ordering level for LNMO in both bilayers is likely driven by the different strain fields experienced by the LNMO layer [28, 29]. Even the slight difference in the transition temperature of the LSMO layer in different bilayer configurations with shifts from 330 K in B-NS to 345 K in B-SN can be also attributed to the effect of strain [30, 31].

This set of bilayers demonstrates that we can change easily the level of cation ordering in LNMO and control the magnetic properties of layers just by changing the layout of the layers in bilayers, but also in more complex heterostructures. This feature provides an interesting avenue to tailor the magnetocaloric behavior close to room temperature, which will be discussed in detail later.

As it is known, MCE strongly depends on the nature of the magnetic phase transition. It should be noted that materials with a first-order magnetic phase tran-

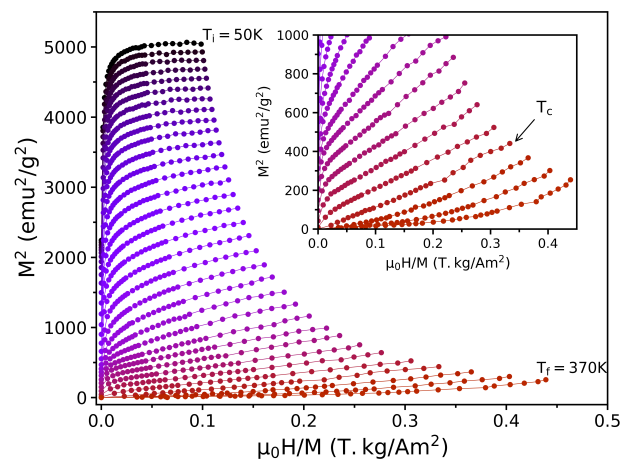


**FIG. 5:** Arrott plots in the temperature range from 50 to 370 K with a temperature interval of 10 K for B-NS sample. The inset of figure shows Arrott plots close to the transition temperature of the sample.

sition usually show a large magnetic entropy change in a very narrow temperature range while their magnetic transition is usually accompanied by large thermal and magnetic hysteresis which neither of them are favorable for magnetic cooling systems [11, 32]. On the other hand, the broad magnetic phase transition and the reversible nature in second-order phase transition materials make them better suited for magnetic cooling systems. So, in order to get a deeper understanding of the nature of magnetic phase transition in our samples, the Arrott plots for the bilayers are derived from isothermal magnetization curves which are measured in the temperature range between 50 to 370 K under to 0–7 T. According to Banerjee's criterion [33], the negative or positive slope of Arrott plots indicate whether the magnetic phase transition is first or second order, respectively. The Arrott plots of the B-NS bilayer sample is depicted in Figure 5 as an example, and it clearly shows a positive slope for the entire temperature range confirming the existence of a second-order magnetic phase transition in our sample. Moreover, the transition temperature of magnetic materials can be extracted using the same plots [34]. Based on the mean-field theory, Arrott plot curves near the transition temperature become straight lines crossing the origin. The inset of Fig. 5 shows the same Arrott plots near the highest transition temperature corresponding to LSMO for that B-NS sample. Similar plots can be found in the supplemental material for the other configurations. From this data, it was found that the highest transition temperature of B-NS and B-SN samples occur at 360 and 340 K, respectively. These transition temperatures from the LSMO layers are in close agreement with the  $M(T)$  measurements. Unfortunately, the lowest transition temperature of LNMO cannot be isolated out of these plots.

In order to determine  $-\Delta S_m$ , Maxwell's relation linking the magnetic entropy change to the bulk magnetization ( $M$ ), the temperature ( $T$ ) and the external magnetic



field ( $B$ ) can be used through the following equation [35]:

$$\left(\frac{\partial S}{\partial B}\right)_{P,T} = \left(\frac{\partial M}{\partial T}\right)_{P,B} \quad (1)$$

In both isothermal and isobaric conditions, the isothermal magnetic entropy change induced by a change in external magnetic field can then be written as:

$$\Delta S_m(T, B_f \rightarrow B_i) = \int_{B_i}^{B_f} \left(\frac{\partial M}{\partial T}\right)_{P,B'} dB' \quad (2)$$

Eq. 2 indicates that the magnetic entropy change is proportional to both the external field variation and the sharpness of a magnetic phase transition. Since magnetization measurements are usually made at discrete field and temperature intervals,  $-\Delta S_m$  can rather be computed using [11]:

$$\Delta S_m(T, B) = \sum_i \frac{M_{i+1} - M_i}{T_{i+1} - T_i} \Delta B_i \quad (3)$$

where  $M_i$  and  $M_{i+1}$  are the magnetization value measured at temperatures  $T_i$  and  $T_{i+1}$ , under a magnetic field changing from 0 to  $B$ , respectively. Thus, Eq. 3 (and Eq. 2) evaluates the surface area between two isothermal magnetization curves measured at  $T_i$  and  $T_{i+1}$  (as presented in Fig. 2 (b)) with  $T$  being their average.

The main scope of this work is to tailor a large and temperature independent magnetic entropy change over a wide temperature range. In order to achieve this goal and make a desirable magnetocaloric material, composite-like bilayer and trilayer structures are chosen as the main route. On top of that, it uses LNMO as a magnetic material with a tunable magnetic transition and combines it within a composite-like structure in the hope of getting a unique magnetocaloric feature. As discussed earlier, the magnetic properties of bilayer samples such as  $T_c$  are affected by changing their layout. So, in this part we inspect to see how this change affects the magnetocaloric properties of bilayer samples.

The calculated isothermal magnetic entropy changes ( $-\Delta S_m$ ) as a function of temperature are shown in Figures 6 (a) and (b) for both bilayer samples under various magnetic field changes up to 7 T. Moreover, the magnetic entropy changes of the monolayers of LNMO and LSMO for  $\mu_0 \Delta H = 5$  T are displayed in the background of Fig. 6 with light blue and grey, respectively. As expected, both bilayer samples exhibit two broad maxima in  $-\Delta S_m$  curves approaching the transition temperatures of each layer. In the B-NS sample (Fig. 6 (a)), these two maxima seen at 235 and 335 K are related to the  $T_c$  of the cation ordered LNMO and the LSMO layers, respectively. The transition temperature of the LNMO layer almost coincides with that of the monolayer of LNMO with a  $T_c$  at 245 K, confirming that the level of cationic ordering

in this layer is not very much affected by the strain from the top LSMO layer. In comparison to the monolayer of LSMO in which the  $T_c$  is at 365 K, the LSMO layer in the B-NS sample experiences a 30-K shift in transition. The difference could originate from the epitaxial strain caused by the bottom LNMO layer leading to a change in the bond length and bond angle of Mn-O-Mn bonds in the  $\text{MnO}_6$  octahedra. The maximum magnetic entropy changes which are attributed to ordered LNMO and LSMO layers are 1.80 and 1.70  $\text{J kg}^{-1} \text{K}^{-1}$  for a magnetic field change of 0-7 T. On the other hand, in the B-SN sample (Fig. 6 (b)), the maximum which is related to the transition of LNMO layer shifts down to 185 K, while the one related to the transition of LSMO increases to 345 K. The significant drop in the  $T_c$  of LNMO can be attributed to the reduction of the cationic ordering level due to the increased epitaxial strain on the LNMO layer, which is in agreement with the trend observed in the XRD data (Fig. 3). Also,  $-\Delta S_m$  reaches a maximum value of 1.76 and 1.42  $\text{J kg}^{-1} \text{K}^{-1}$  for LNMO and LSMO layers under  $\mu_0 \Delta H = 7$  T, respectively.

As noticed, both bilayer samples show a large magnetic entropy change which barely varies over a wide temperature range. The full width at half maximum is about 250 K for both samples (from  $\sim 115$  K to above room temperature at  $\sim 365$  K). Unlike the other approaches used to tune the magnetic properties and especially the MCE such as doping or changing the growth conditions, this composite-like approach allows one to widen the magnetic entropy change without sacrificing much of the  $\Delta S_m$  magnitude. In the next section we show how  $\Delta S_m$  can be further improved in terms of intensity and temperature span by adding another layer to the composites structure. Of course, we will show that strain can be used to our advantage as was done with bilayers.

## B. Trilayers

As seen in the previous section, we can take advantage of the sensitivity of cation ordering to strain of LNMO in multilayer samples just by changing the stacking order of the layers. This effect originates from different lattice mismatches between the layers and the substrate. It provides an opportunity to control the magnetic and magnetocaloric properties of more complex heterostructures and tailor a large MCE over a wide temperature range. As a proof of concept, trilayer samples with LNMO-LSMO-LNMO and LSMO-LNMO-LSMO configurations are compared.

Figure 7 shows field-cooled (FC) magnetization as a function of temperature under a fixed magnetic field of 200 Oe for both trilayer samples. As expected, T-NSN sample exhibits three magnetic phase transitions at roughly 155, 230 and 335 K. This is confirmed in particular using the derivative  $dM/dT$  as shown in the inset of Fig. 7. The first transition at 155 K comes from the top LNMO layer experiencing strain similar to that in the

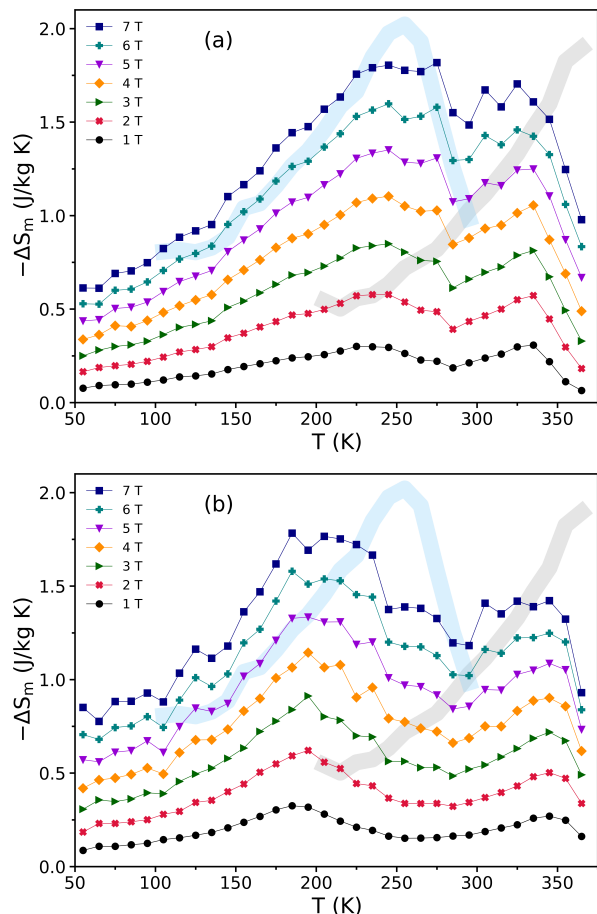


**FIG. 6:** The magnetic entropy change as a function of temperature for different magnetic field variations for (a) B-NS and (b) B-SN samples. The light blue and grey curves on the background show the  $-\Delta S_m$  as a function of temperature at a magnetic field of 5 T for monolayers of LNMO and LSMO.

B-SN sample. The second magnetic transition at 230 K comes from the bottom LNMO layer in direct contact with the substrate as was observed in the B-NS bilayer. Finally, the transition at 335 K is related to the LSMO layer sitting between two LNMO, consistent also with its  $T_c$  observed in the B-NS bilayer. In the other trilayer sample (T-SNS), we observe only two magnetic phase transitions in the  $M(T)$  curve at 180 and 340 K. The LSMO layers show a  $T_c$  at 340 K and the middle LNMO layer has a  $T_c$  at 180 K. This value of  $T_c \sim 180$  K indicates that it has almost the same level of cationic ordering as what we have observed for LNMO in B-SN sample.

In a trilayer sample with two LNMO layers, we can have both disordered and highly ordered LNMO phases simultaneously in the sample from the top and bottom layers experiencing different strain fields. As a result, trilayer samples with the T-NSN configuration gives three different transitions which covers quite a large temperature range starting from 155 to 335 K. With an appropriate choice of thicknesses for each layer, one could get

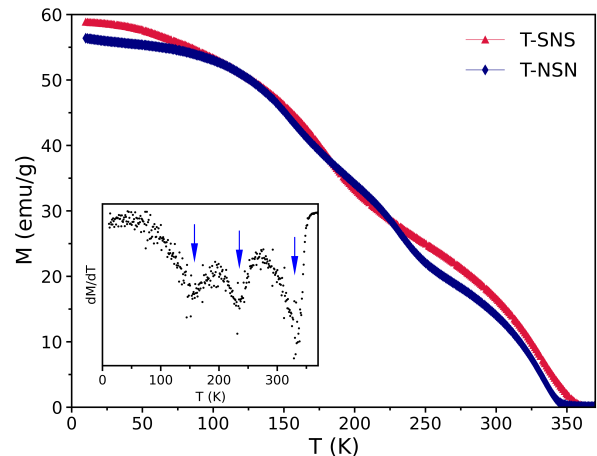


**FIG. 7:** Magnetization as a function of temperature under a magnetic field of 200 Oe for the trilayer samples. The inset shows the derivative of the magnetization with respect to the temperature for the T-NSN sample. The transitions are indicated with blue arrows.

a temperature-independent table-top magnetic entropy change over a wide temperature range close to room temperature.

As mentioned before, one of the biggest advantage of SOMT materials is their small thermal and magnetic hysteresis. In Figure 8 (a), the magnetization as a function of magnetic field was measured for a T-NSN sample at the transition temperature of each layer and at 10 K. The sample saturates very quickly at low magnetic field, and also it exhibits a very low coercive field of 160 Oe at 10 K and this value decreases to roughly 10 Oe at 335 K (Fig. 8 (b)). The same is observed for the T-SNS sample (see supplemental material).

Magnetic isotherms measurements are carried out in the temperature range going from 50 to 370 K to determine Arrott plots and magnetic entropy changes for both trilayer samples. Similar to bilayers, an example of Arrott plots measurements for trilayers is shown in Figure 9. All  $M^2$  vs.  $H/M$  curves of the T-SNS sample show positive slopes in the entire temperature range which indicates that the sample undergoes a second-order magnetic phase transition. A similar trend can be observed in the Arrott plots of the other trilayer (T-NSN, see supplemental material). Furthermore, in order to determine the  $T_c$  of the samples, the Arrott plots close to the transition temperature of T-SNS multilayer is depicted in the inset of Fig. 9. It is found that the transition of T-SNS and T-NSN samples occur at 350 and 340 K, respectively. As we saw in the bilayer samples, these two transitions are those of the LSMO layers in agreement with the  $M(T)$  measurements in Fig. 7.

Magnetic entropy changes as a function of temperature taken at different magnetic fields for the two trilayer samples are plotted in Figures 10 (a) and (b). At the transition temperature of each layer, there is a broad

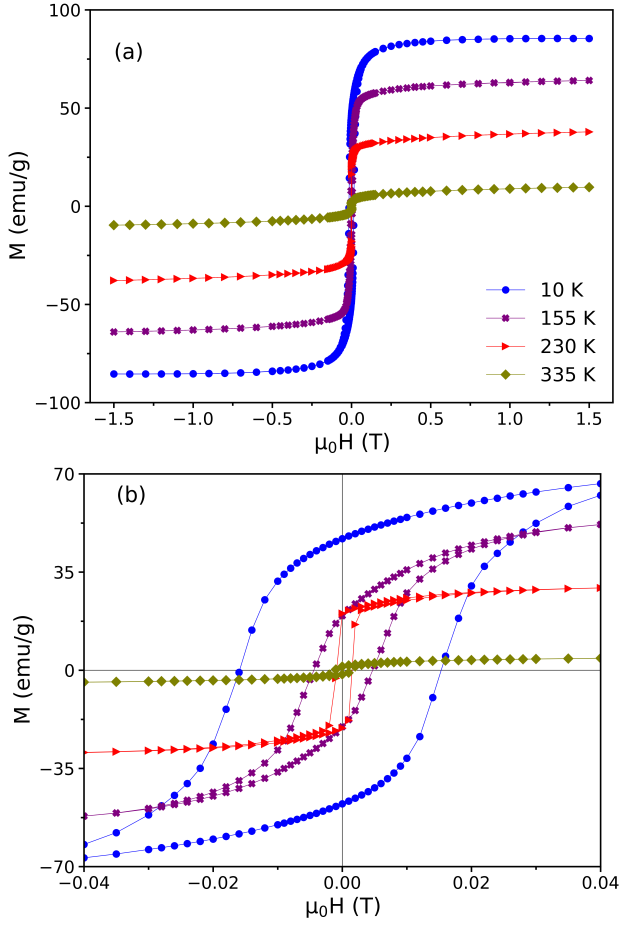


**FIG. 8:** (a) Magnetization as a function of magnetic field for a T-NSN sample at 10, 155, 230 and 335 K. (b) The hysteresis loops at low field showing the small coercive fields.

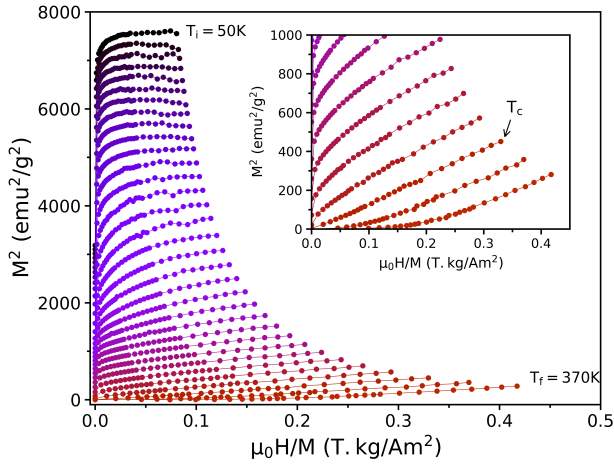


**FIG. 9:** Arrott plots of T-NSN sample in the temperature range between 50 and 370 K. The inset shows Arrott plots close to the  $T_c$  of the LSMO layer.

maximum in  $\Delta S_m$  that comes from the magnetic phase transitions occurring at the transition temperatures of each layer. For instance, the T-SNS sample (Fig. 10 (a)) exhibits two peaks in  $\Delta S_m$  curves at 185 and 335 K which correspond to the magnetic transition of LNMO and two LSMO layers, respectively. The maximum values of  $-\Delta S_m$  corresponding to LNMO and LSMO layers are  $1.56$  and  $2.03 \text{ J kg}^{-1} \text{ K}^{-1}$  for  $\mu_0 \Delta H = 7 \text{ T}$ . As shown in Fig. 10 (b), the other trilayer sample (T-NSN) shows three peaks in  $\Delta S_m$  curves due to the existence of different magnetic phases in two LNMO layers. They can be better observed for low applied field (1 and 2 T). For this layer configuration, the peaks are located at 175, 245 and 345 K which are related to the transition of disordered LNMO layer (the top layer), the cation-ordered LNMO layer (the bottom layer) and the LSMO middle layer, respectively. For  $\mu_0 \Delta H = 7 \text{ T}$ ,  $-\Delta S_m$  shows a maximum of  $2.21$ ,  $2.21$  and  $1.42 \text{ J kg}^{-1} \text{ K}^{-1}$  that correspond to disordered LNMO, ordered LNMO and LSMO layers, respectively.

It must be emphasized that the large magnetic entropy changes with a wide operating temperature range ( $\delta T_{\text{FWHM}} = 260 \text{ K}$ ) which go slightly above room temperature would make these multilayer composites an interesting candidate for magnetic cooling systems at room temperature. In addition, both trilayer samples show a fairly flat and temperature-independent  $\Delta S_m$  within the mid-range temperature which can extend over  $\Delta T \sim 100 \text{ K}$  under  $\mu_0 \Delta H = 5 \text{ T}$  (Figs. 10). This temperature independent  $\Delta S_m$  over a wide temperature window would make these two trilayer samples suitable candidates for AMR refrigeration [36]. Moreover, with an appropriate choice of thicknesses for each layer (for example a bit thicker for LSMO) one could likely generate a constant  $-\Delta S_m$  from 175 to 335 K.

A useful tool which allows usually to compare the cooling performances of magnetocaloric materials is the relative cooling power ( $RCP$ ).  $RCP$  is the amount of heat transfer between the cold and hot reservoirs in one refrigeration cycle and it is defined as:

$$RCP = -\Delta S_m(\text{max}) \times \delta T_{\text{FWHM}} \quad (4)$$

$RCP$  is not only considering the amplitude of the magnetic entropy change  $\Delta S_m(\text{max})$ , but it also takes into account the working temperature range  $\delta T_{\text{FWHM}}$  which is a key parameter in magnetic cooling systems.  $RCP$  is mostly used for materials with a single transition which have a fairly symmetric peak in  $\Delta S_m(T)$  curves. However, in the case of composites and materials with more than one transition, refrigerant capacity ( $\mathcal{RC}$ ) is usually employed [21, 37].  $\mathcal{RC}$  is specified as the area under the curve of  $\Delta S_m$  between the temperatures which correspond to half maximum [38]:

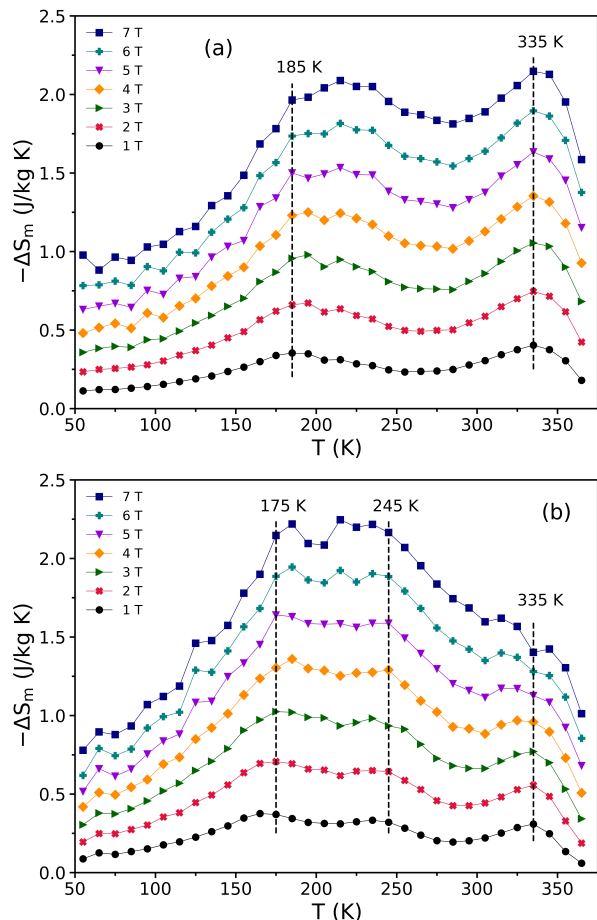


**FIG. 10:** Temperature dependence of the magnetic entropy change of (a) T-SNS and (b) T-NSN samples under various magnetic field changes.

$$\mathcal{RC} = - \int_{T_C}^{T_H} \Delta S_m(T) dT \quad (5)$$

Figure 11 presents the  $\mathcal{RC}$  values as a function of magnetic field for all four samples and also that of gadolinium as a reference to compare with our samples. All samples show a relatively large  $\mathcal{RC}$  with an almost linear magnetic field dependence. The values of  $\mathcal{RC}$  reach 273, 264, 259 and 335  $\text{J kg}^{-1}$  for B-SN, B-NS, T-SNS and T-NSN under a magnetic field of 5 T, respectively. By comparing with Gadolinium as a reference [39], it can be seen that the value of  $\mathcal{RC}$  for T-NSN sample is about 82% of Gd for  $\mu_0\Delta H = 5$  T. All the values of  $\Delta S_m$  and  $\mathcal{RC}$  for our samples under different magnetic fields are listed in Table I. Among other families with comparable  $\mathcal{RC}$  to Gd, such as  $\text{La}(\text{FeSi})_{13}$ -based [40, 41] and  $\text{Gd}_5(\text{SiGe})_4$ -based [42] compounds, our multilayer samples have additional advantages over other candidates such as wide working temperature range and a second order magnetic phase transition. Our results confirm that the composite approach combining 3d metals oxides such

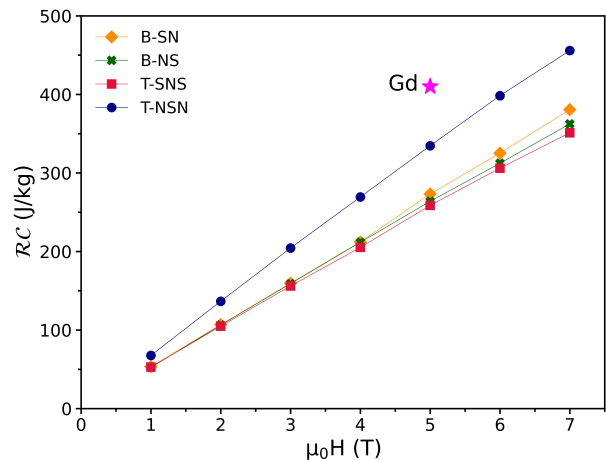


**FIG. 11:** Refrigerant capacity ( $\mathcal{RC}$ ) as a function of magnetic field for all samples.  $\mathcal{RC}$  of gadolinium is shown for comparison [39].

as manganites and double perovskites is a promising path to produce performant cooling devices based on the magnetocaloric effect.

$$\mathcal{RC} = - \int_{T_C}^{T_H} \Delta S_m(T) dT \quad (6)$$

#### IV. CONCLUSION

In this work, we obtain a large and almost temperature independent magnetocaloric effect extending from 175 K up to room temperature in multilayer composites of LNMO and LSMO. We take advantage of the sensitivity of cationic ordering to strain in LNMO layers to achieve multilayers with multiple magnetic transitions. For this purpose, two series of bilayer samples with different layouts of LSMO-LNMO and LNMO-LSMO, and two series of trilayer samples with layouts of LSMO-LNMO-LSMO and LNMO-LSMO-LNMO are prepared. All the samples show a large  $\Delta S_m$  over a wide temperature range, as large as 260 K, which extends above room temperature. The maximum value of  $-\Delta S_m$  in the trilayer samples is found to be 2.03 and 2.21  $\text{J kg}^{-1} \text{K}^{-1}$  under a magnetic field change of 7 T in T-SNS and T-NSN samples, respectively. Moreover, the trilayer samples reveal an almost temperature independent magnetic entropy change that can extend over a large temperature range of  $\Delta T \cong 100$  K. The refrigerant capacity ( $\mathcal{RC}$ ) reaches a maximum value of 259 and 335  $\text{J kg}^{-1}$  for  $\mu_0\Delta H = 5$  T in T-SNS and T-NSN samples, respectively. These large values of  $\mathcal{RC}$  in our composite-like multilayers are comparable to Gd and other reference materials. Our results demonstrate that a composite route to design new materials for magnetic cooling systems is a promising path.



Sample	$-\Delta S_m$ (J kg <sup>-1</sup> K <sup>-1</sup> )			$\mathcal{RC}$ (J kg <sup>-1</sup> )		
	2 T	5 T	7 T	2 T	5 T	7 T
B-SN	0.62	1.33	1.76	106.82	273.23	380.62
B-NS	0.57	1.35	1.80	106.31	263.81	362.39
T-SNS	0.68	1.50	2.03	104.91	258.61	351.14
T-NSN	0.70	1.63	2.21	136.61	334.57	455.82

**TABLE I:** The values of  $-\Delta S_m$  and  $\mathcal{RC}$  for all four multilayers under different magnetic fields.

### ACKNOWLEDGMENT

The authors thank B. Rivard, S. Pelletier and M. Dion for technical support. The authors would also like to thank P. Brojabasi for preparing the initial samples. This

work is supported by the Natural Sciences and Engineering Research Council of Canada (NSERC) under grant RGPIN-2018-06656, the Canada First Research Excellence Fund (CFREF), the Fonds de Recherche du Québec - Nature et Technologies (FRQNT) and the Université de Sherbrooke. M.B. acknowledges the financial support from the International University of Rabat.

- 
- [1] Balli, M., Jandl, S., Fournier, P., and Kedous-Lebouc, A. *Appl. Phys. Rev.* **4**(2), 021305 (2017).
- [2] Gschneidner Jr, K. A., Pecharsky, V., and Tsokol, A. *Rep. Prog. Phys.* **68**(6), 1479 (2005).
- [3] Weiss, P. and Piccard, A. *J. Phys. Theor. Appl.* **7**(1), 103–109 (1917).
- [4] Brown, G. *J. Appl. Phys.* **47**(8), 3673–3680 (1976).
- [5] Pecharsky, V. K. and Gschneidner Jr, K. A. *Phys. Rev. Lett.* **78**(23), 4494 (1997).
- [6] Xu, Z., Lin, G., and Chen, J. *J. Alloys Compd.* **639**, 520–525 (2015).
- [7] Balli, M., Rosca, M., Fruchart, D., and Gignoux, D. *J. Magn. Magn. Mater.* **321**(2), 123–125 (2009).
- [8] Fujieda, S., Fujita, A., and Fukamichi, K. *Appl. Phys. Lett.* **81**(7), 1276–1278 (2002).
- [9] Fujita, A., Fujieda, S., Fukamichi, K., Mitamura, H., and Goto, T. *Phys. Rev. B* **65**(1), 014410 (2001).
- [10] Tokura, Y. and Tomioka, Y. *J. Magn. Magn. Mater.* **200**(1-3), 1–23 (1999).
- [11] Phan, M.-H. and Yu, S.-C. *J. Magn. Magn. Mater.* **308**(2), 325–340 (2007).
- [12] Mira, J., Rivas, J., Hueso, L., Rivadulla, F., and Lopez Quintela, M. *J. Appl. Phys.* **91**(10), 8903–8905 (2002).
- [13] Balli, M., Fournier, P., Jandl, S., Truong, K., and Gospodinov, M. *J. Appl. Phys.* **116**(7), 073907 (2014).
- [14] Brahiti, N., Abbasi Eskandari, M., Balli, M., Gauvin-Ndiaye, C., Nourafkan, R., Tremblay, A.-M., and Fournier, P. *J. Appl. Phys.* **127**(11), 113905 (2020).
- [15] Kobayashi, K.-I., Kimura, T., Sawada, H., Terakura, K., and Tokura, Y. *Nature* **395**(6703), 677–680 (1998).
- [16] Anderson, P. W. *Solid State Phys.* **14**, 99–214 (1963).
- [17] Kanamori, J. *J. Phys. Chem. Solids* **10**(2-3), 87–98 (1959).
- [18] Singh, M., Truong, K., Jandl, S., and Fournier, P. *J. Appl. Phys.* **107**(9), 09D917 (2010).
- [19] Iliev, M., Gospodinov, M., Singh, M., Meen, J., Truong, K., Fournier, P., and Jandl, S. *J. Appl. Phys.* **106**(2), 023515 (2009).
- [20] Bull, C., Gleeson, D., and Knight, K. *J. Phys.: Condens. Matter* **15**(29), 4927 (2003).
- [21] Matte, D., de Lafontaine, M., Ouellet, A., Balli, M., and Fournier, P. *Phys. Rev. Applied* **9**(5), 054042 (2018).
- [22] Rebello, A., Naik, V., and Mahendiran, R. *J. Appl. Phys.* **110**(1), 013906 (2011).
- [23] Zhong, X., Shen, X., Mo, H., Jiao, D., Liu, Z., Qiu, W., Zhang, H., and Ramanujan, R. *Mater. Today Commun.* **14**, 22–26 (2018).
- [24] Zhang, Y., Yang, Y., Xu, X., Geng, S., Hou, L., Li, X., Ren, Z., and Wilde, G. *Sci. Rep.* **6**(1), 1–9 (2016).
- [25] Tian, H., Zhong, X., Liu, Z., Zheng, Z., and Min, J. *Mater. Lett.* **138**, 64–66 (2015).
- [26] Guo, Y., Shi, L., Zhou, S., Zhao, J., and Liu, W. *Appl. Phys. Lett.* **102**(22), 222401 (2013).
- [27] Ettayfi, A., Moubah, R., Boutahar, A., Hlil, E., and Lassri, H. *J. Supercond Nov Magn* **29**(1), 133–138 (2016).
- [28] Wu, S.-Q., Cheng, S., Lu, L., Liu, M., Jin, X.-W., Cheng, S.-D., and Mi, S.-B. *Sci. Rep.* **8**(1), 1–9 (2018).
- [29] Jin, X.-W., Lu, L., Mi, S.-B., Liu, M., and Jia, C.-L. *Appl. Phys. Lett.* **109**(3), 031904 (2016).
- [30] Dey, P., Nath, T., and Taraphder, A. *Appl. Phys. Lett.* **91**(1), 012511 (2007).
- [31] Wang, B., You, L., Ren, P., Yin, X., Peng, Y., Xia, B., Wang, L., Yu, X., Mui Poh, S., Yang, P., et al. *Nat. Commun.* **4**(1), 1–7 (2013).
- [32] Smith, A., Bahl, C. R., Bjørk, R., Engelbrecht, K., Nielsen, K. K., and Pryds, N. *Adv. Energy Mater.* **2**(11), 1288–1318 (2012).
- [33] Banerjee, B. *Physics Letters* **12**(1), 16–17 (1964).
- [34] Arrott, A. *Phys. Rev.* **108**(6), 1394 (1957).
- [35] Tishin, A. M. and Spichkin, Y. I. *The magnetocaloric effect and its applications.* CRC Press, (2016).

- [36] Franco, V., Blázquez, J., Ipus, J., Law, J., Moreno-Ramírez, L., and Conde, A. *Prog. Mater. Sci.* **93**, 112–232 (2018).
- [37] Zhou, L., Tang, Y., Chen, Y., Guo, H., Pang, W., and Zhao, X. *J. Rare Earths* **36**(6), 613–618 (2018).
- [38] Gschneidner Jr, K., Pecharsky, V., Pecharsky, A., and Zimm, C. *Materials Science Forum* **315**, 69–76 (1999).
- [39] Dan’Kov, S. Y., Tishin, A., Pecharsky, V., Gschneidner, K., et al. *Phys. Rev. B* **57**(6), 3478 (1998).
- [40] Shamba, P., Zeng, R., Wang, J., Campbell, S., and Dou, S. *J. Magn. Magn. Mater.* **331**, 102–108 (2013).
- [41] Shamba, P., Debnath, J., Zeng, R., Wang, J., Campbell, S. J., Kennedy, S., and Dou, S. *J. Appl. Phys.* **109**(7), 07A940 (2011).
- [42] Provenzano, V., Shapiro, A. J., and Shull, R. D. *Nature* **429**(6994), 853–857 (2004).

## Supplemental material

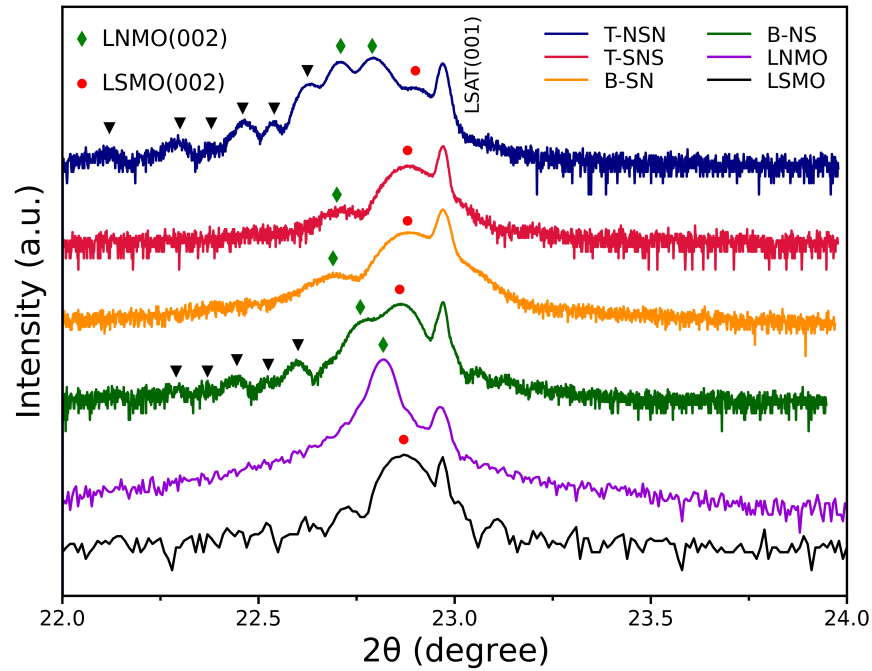
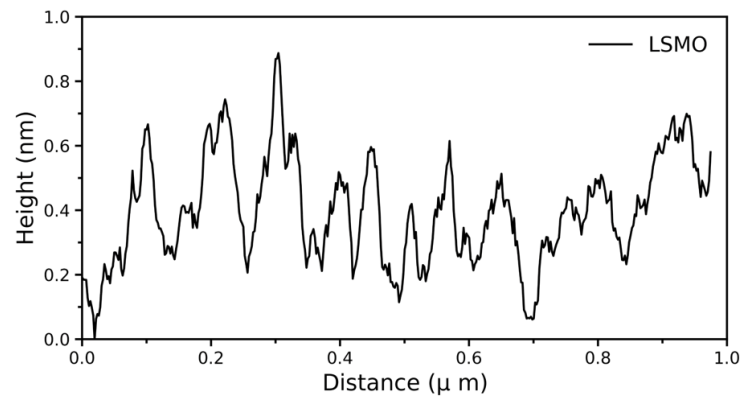
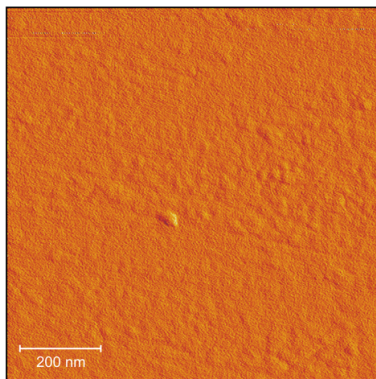
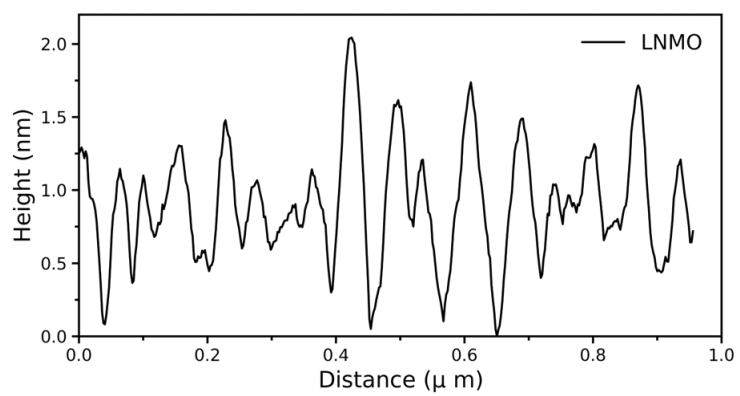
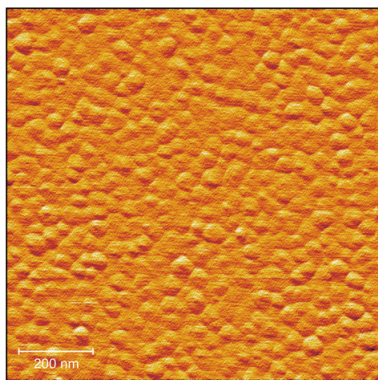


**FIG. 12:** X-ray diffraction patterns around the (001) Bragg peak of the substrate from  $2\theta = 22^\circ$  to  $24^\circ$ . From bottom to top: the monolayers of LSMO and LNMO, bilayers of B-NS and B-SN, and trilayers of T-SNS and T-NSN. Laue oscillations are specified with (▼). Diamonds indicate the diffraction peaks of LNMO and solid circles for LSMO.

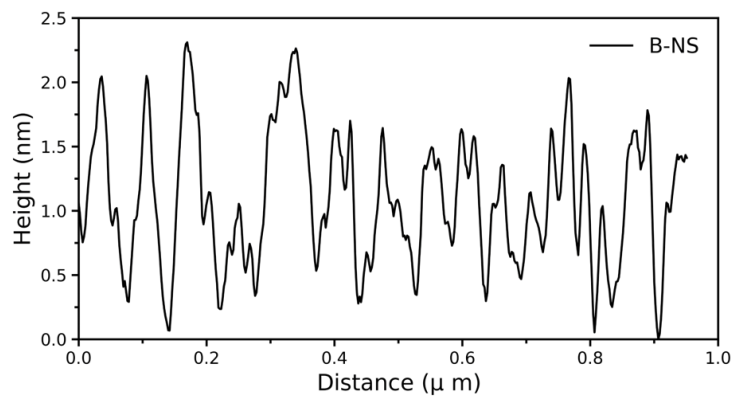
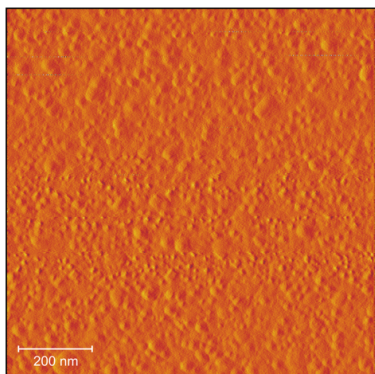
(a)



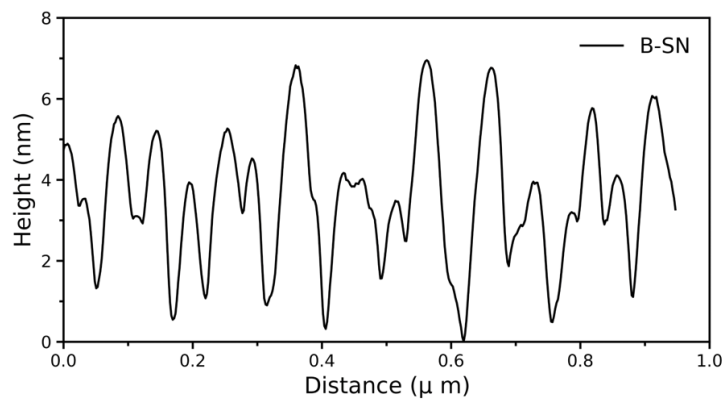
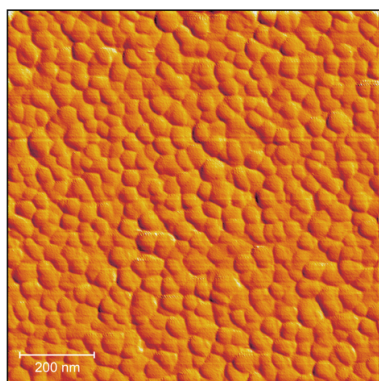
(b)



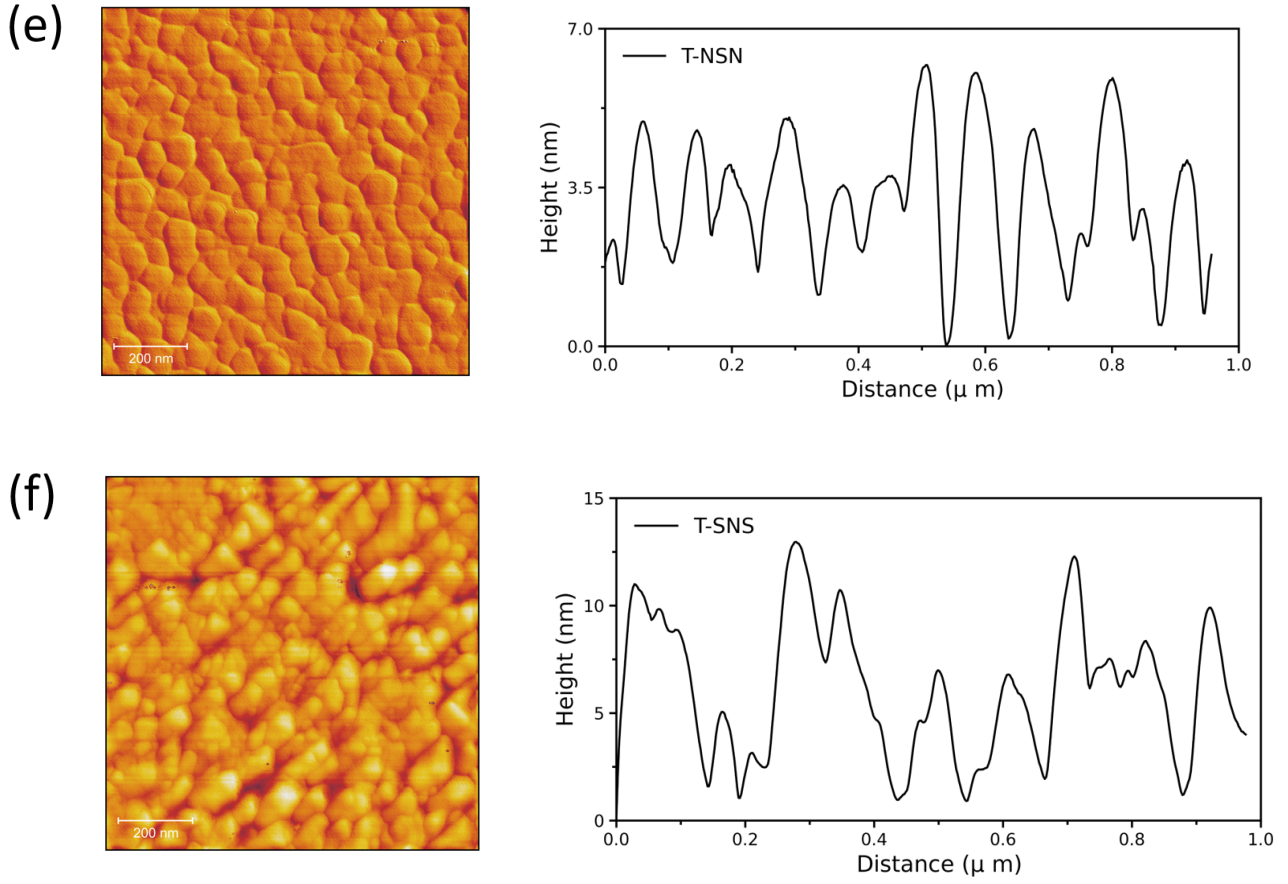
(c)



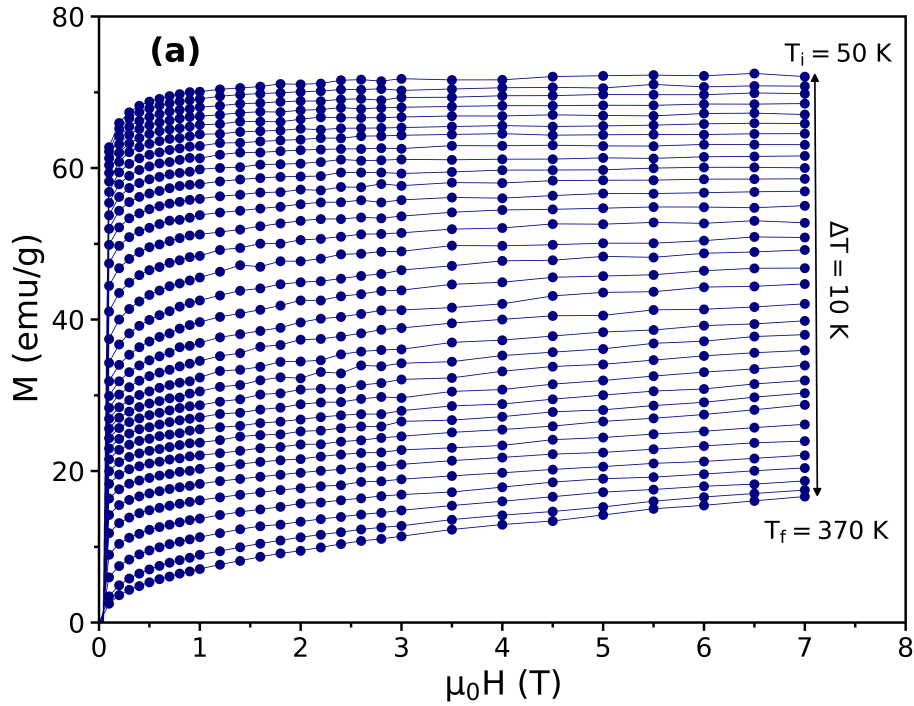
(d)







**FIG. 13:** AFM images (left) and height profiles (right) for a line drawn across the AFM images for (a) monolayer of LSMO, (b) monolayer of LNMO, (c) bilayer of B-NS, (d) bilayer of B-SN, (e) trilayer of T-NSN and (f) trilayer of T-SNS. The measurements were carried out using a Veeco Dimension Icon Atomic Force Microscope (AFM).



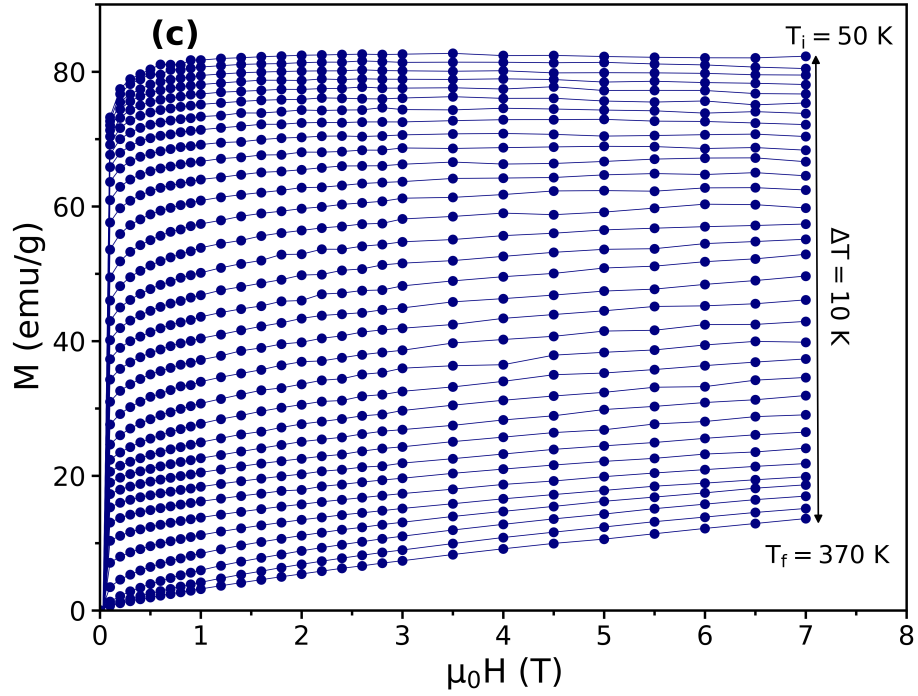
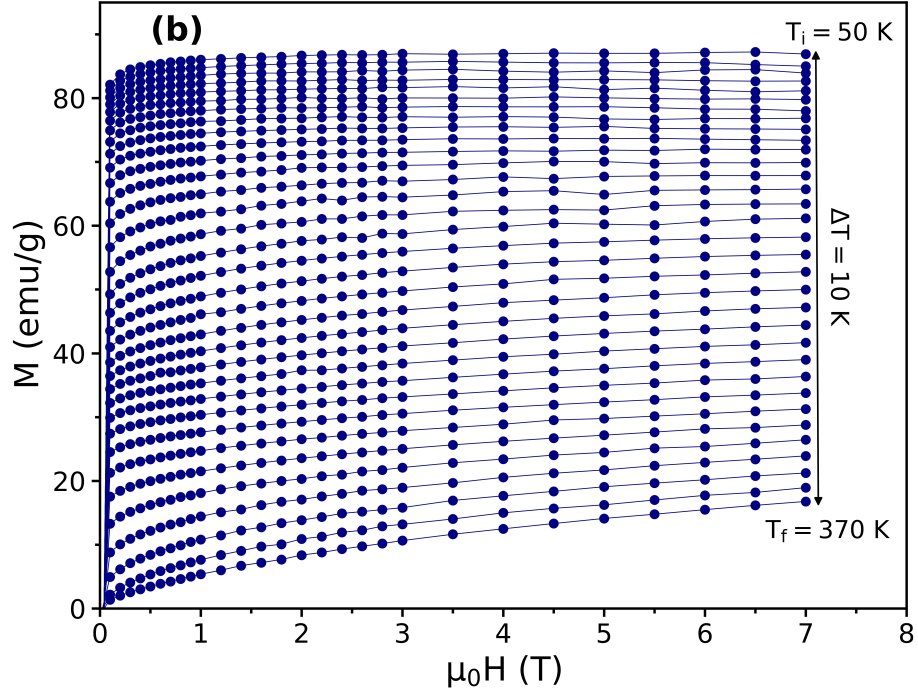


**FIG. 14:** Isothermal magnetization curves as a function of magnetic field in the temperature range from 50 to 370 K with a temperature interval of 10 K for (a) B-SN, (b) T-SNS and (c) T-NSN samples. These data are obtained after the subtraction of the diamagnetic background from the substrate and the sample holder.

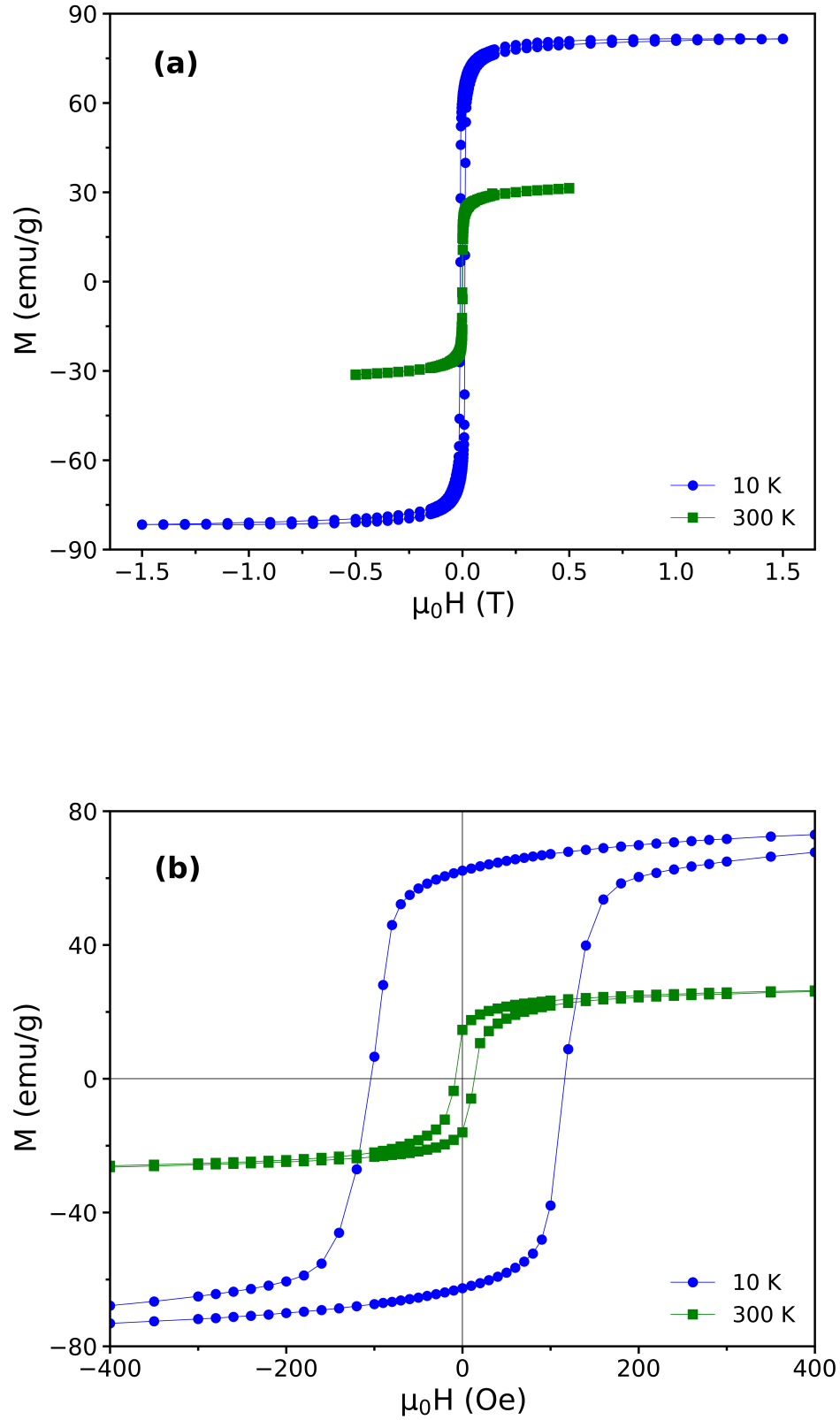


**FIG. 15:** (a) Magnetic hysteresis loop measured at 10 and 300 K for T-SNS sample. (b) Magnified view around zero field showing the coercive field and the remnant magnetization at 10 and 300 K.

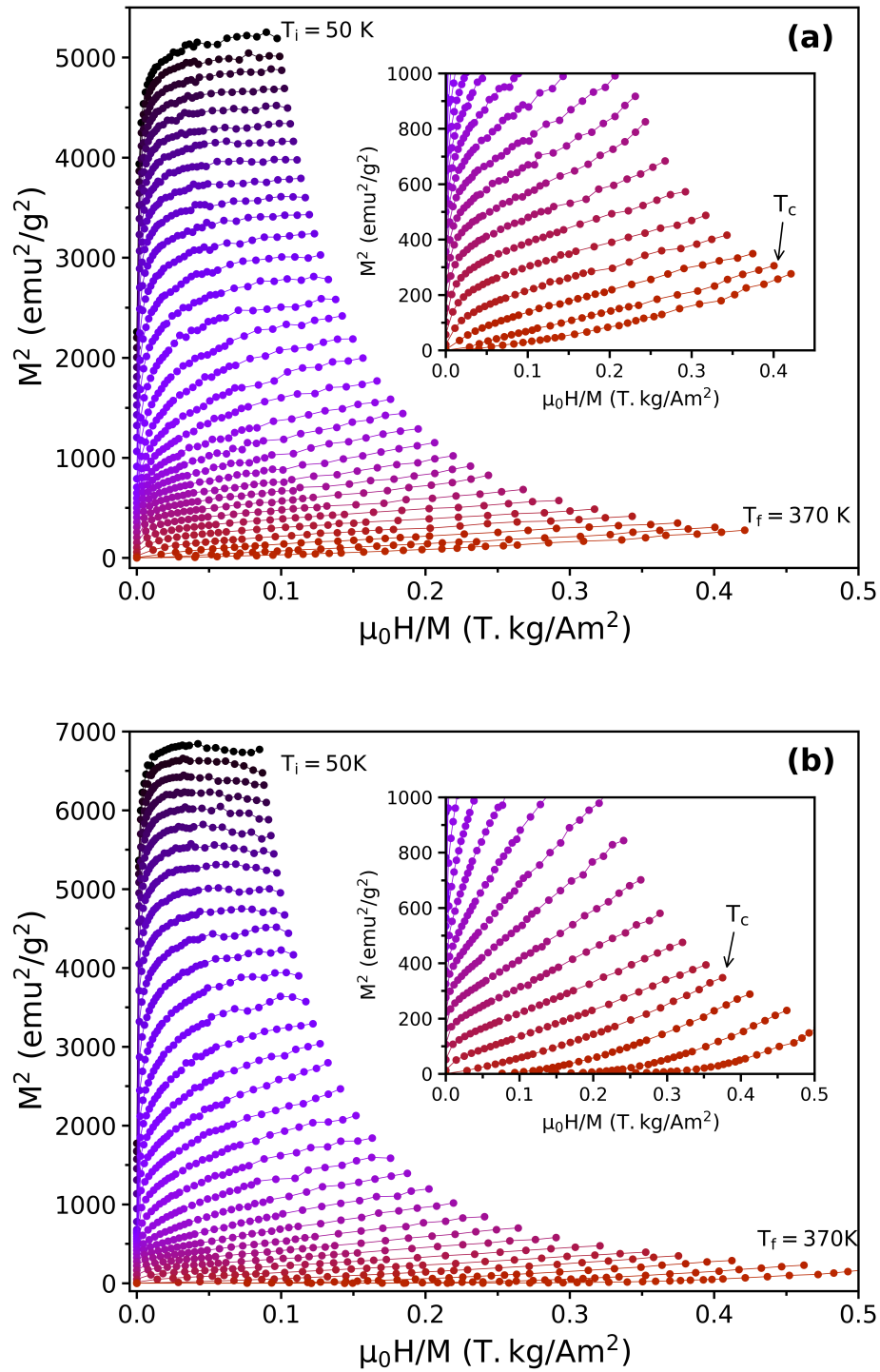


**FIG. 16:** The Arrott plots in the temperature range from 50 to 370 K with a temperature interval of 10 K for (a) B-SN and (b) T-NSN samples. Inset shows a magnified view around the transition temperature of the LSMO layer.